

The design and construction of a high-resolution velocity-map imaging apparatus for photoelectron spectroscopy studies of size-selected clusters

Iker León, Zheng Yang, Hong-Tao Liu, and Lai-Sheng Wang

Citation: [Review of Scientific Instruments](#) **85**, 083106 (2014); doi: 10.1063/1.4891701

View online: <http://dx.doi.org/10.1063/1.4891701>

View Table of Contents: <http://scitation.aip.org/content/aip/journal/rsi/85/8?ver=pdfcov>

Published by the [AIP Publishing](#)

Articles you may be interested in

[Note: A novel dual-channel time-of-flight mass spectrometer for photoelectron imaging spectroscopy](#)
Rev. Sci. Instrum. **84**, 066108 (2013); 10.1063/1.4811739

[Slow photoelectron velocity-map imaging spectroscopy of the vinoxide anion](#)
J. Chem. Phys. **130**, 244309 (2009); 10.1063/1.3157208

[A versatile electron-ion coincidence spectrometer for photoelectron momentum imaging and threshold spectroscopy on mass selected ions using synchrotron radiation](#)
Rev. Sci. Instrum. **80**, 023102 (2009); 10.1063/1.3079331

[Velocity-map imaging electron spectrometer with time resolution](#)
Rev. Sci. Instrum. **75**, 324 (2004); 10.1063/1.1642749

[High-resolution state-selected ion-molecule reaction studies using pulsed field ionization photoelectron-secondary ion coincidence method](#)
Rev. Sci. Instrum. **74**, 4096 (2003); 10.1063/1.1599071

ZABER



Automate your research applications with Zaber's line of high precision positioning devices.

Low cost. Built-in controllers. Simple to set up and easy to use.

[Learn more at zaber.com](http://zaber.com) ►

The design and construction of a high-resolution velocity-map imaging apparatus for photoelectron spectroscopy studies of size-selected clusters

Iker León,^{a)} Zheng Yang, Hong-Tao Liu,^{b)} and Lai-Sheng Wang^{c)}

Department of Chemistry, Brown University, Providence, Rhode Island 02912, USA

(Received 11 May 2014; accepted 18 July 2014; published online 7 August 2014)

A new velocity-map imaging apparatus equipped with a laser-vaporization supersonic cluster source and a time-of-flight mass spectrometer is described for high-resolution photoelectron spectroscopy studies of size-selected cluster anions. Vibrationally cold anion clusters are produced using a laser-vaporization supersonic cluster source, size-selected by a time-of-flight mass spectrometer, and then focused co-linearly into the interaction zone of the high-resolution velocity-map imaging (VMI) system. The multilens VMI system is optimized via systematic simulations and can reach a resolution of 1.2 cm^{-1} (FWHM) for near threshold electrons while maintaining photoelectron kinetic energy resolutions ($\Delta KE/KE$) of $\sim 0.53\%$ for higher energy electrons. The new VMI lens has superior focusing power over a large energy range, yielding highly circular images with distortions no larger than 1.0025 between the long and short radii. The detailed design, simulation, construction, testing, and performance of the high-resolution VMI apparatus are presented. © 2014 AIP Publishing LLC. [<http://dx.doi.org/10.1063/1.4891701>]

I. INTRODUCTION

The imaging technique was first developed by Chandler and Houston in 1987 to record spatial distributions of photodissociation products¹ and was soon applied to photoelectrons from multiphoton ionization of Xe and size-selected cluster anions.^{2,3} However, the resolution attainable in the early efforts was quite limited. A major advance was achieved in 1997 when Eppink and Parker developed the so-called “velocity-map imaging” (VMI) lens, using a combination of ion lens optics, that significantly improved the resolution of the imaging method.⁴ Anion photoelectron spectroscopy (PES) is a powerful technique for the study of size-selected atomic clusters, probing directly the electronic structure of the corresponding neutral species. However, the resolution of PES is limited to a few meV in the best cases, which is not sufficient to resolve low frequency vibrations. The introduction of VMI into PES of size-selected anions^{5–7} has made it into a powerful alternative PES method over the past decade.^{8–13} The advantage of photoelectron imaging lies at its high detection efficiency while yielding photoelectron angular information at the same time. The ability to detect very low energy electrons makes VMI potentially a much higher resolution method for PES.

Until recently, the electron kinetic energy (KE) resolution of VMI in anion PES was limited to $\Delta KE/KE \sim 2\%$.^{8,14} Although this resolution was better than conventional PES for low energy electrons, there was room for further improvement. In 2007, Cavanagh and co-workers presented a VMI

lens design with superior resolution.¹⁵ Their design achieved an energy resolution of $\Delta KE/KE = 0.38\%$ for 0.87 eV electrons, resolving six spin-orbit transitions for O^- photodetachment and illustrating the high resolution potential of VMI. The effective photoelectron energy resolution was shown to be 3.3 meV (or 27 cm^{-1} FWHM) for 0.87 eV electrons, although the performance for low energy electrons was not described. On the other hand, the sensitivity of the imaging method to slow-electrons has been used by the Neumark group to achieve high energy resolution for near zero-eV (or near threshold) electrons, which they called “slow electron velocity-map imaging (SEVI).”^{14,16} They achieved an impressive line width for near threshold electrons as low as 1.5 cm^{-1} for photodetachment of Cl^- using low extraction voltages in the SEVI mode,¹⁶ whereas the lowest peak width achieved for a molecular system was 4.1 cm^{-1} for photoelectrons with 13 cm^{-1} kinetic energy for photodetachment of cold C_5^- .¹⁷

We have used PE imaging to study multiply charged anions from an electrospray ion source.^{10,18,19} Over the past few years, we have been developing a high-resolution PE imaging system for the study of size-selected cluster anions produced from a laser vaporization supersonic cluster source. It has been fully tested and has yielded some very interesting initial results.^{20–23} The new VMI system is based on a previous photoion-imaging strategy that highlight how weak fields in the electrostatic lenses during the initial acceleration stage allow achieving a better velocity focusing at the cost of sacrificing temporal focusing.²⁴ Our new VMI system can reach a resolution of 1.2 cm^{-1} for near threshold electrons comparable to that reported by Neumark,¹⁶ while still maintaining good energy resolution ($\Delta KE/KE \sim 0.53\%$) for higher energy electrons comparable to that reported by Cavanagh and co-workers.¹⁵ Furthermore, we have achieved almost circular images that do not require any symmetrization treatment before inverse-Abel transformation. Our lens design also allows

^{a)}Present address: Departamento de Química Física, Facultad de Ciencia y Tecnología, Universidad del País Vasco-UPV/EHU, B. Sarriena s/n, Leioa 48940, Spain.

^{b)}Present address: Division of Radiochemistry Engineering and Technology, Shanghai Institute of Applied Physics, Chinese Academy of Sciences, Shanghai 201800, China.

^{c)}E-mail: Lai-Sheng_Wang@brown.edu

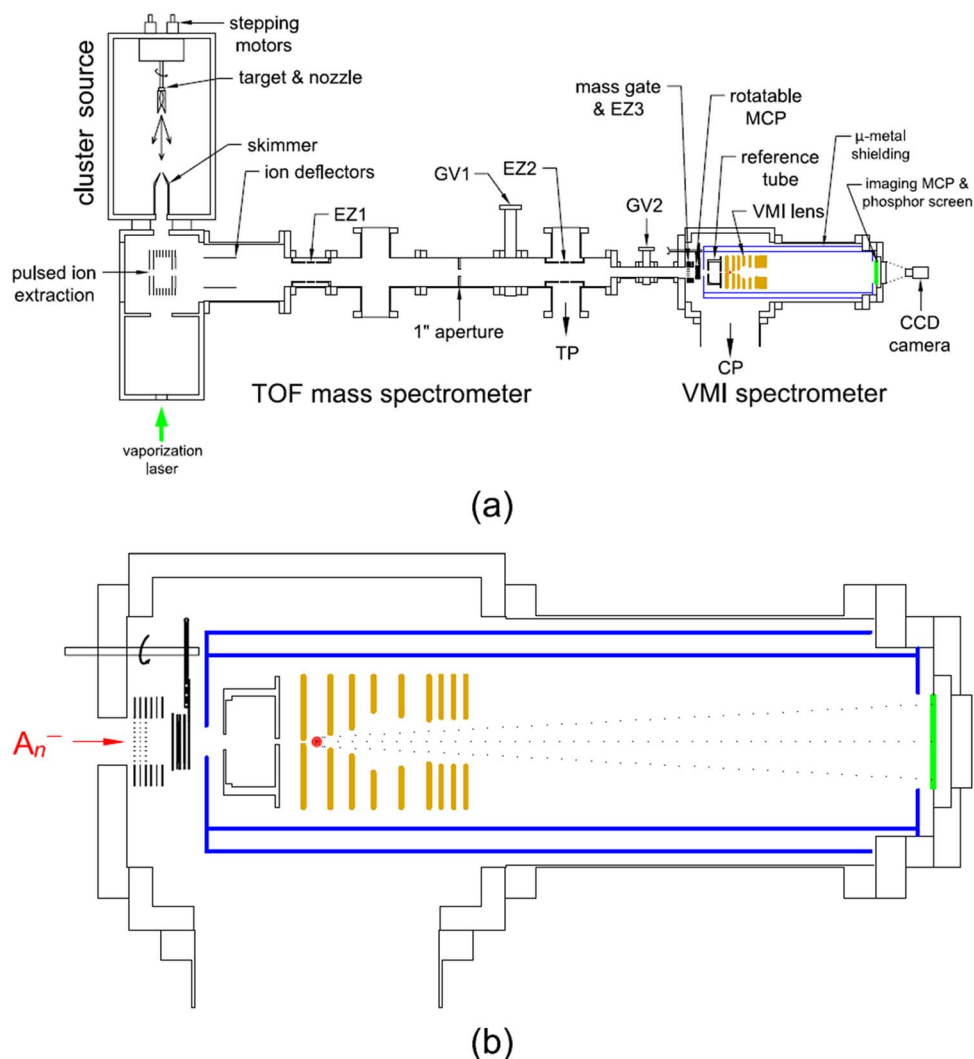


FIG. 1. (a) Overall schematic view of the high-resolution photoelectron spectroscopy apparatus for size-selected clusters using velocity-map imaging (VMI). (b) Expanded view of the optimized high-resolution VMI spectrometer. The red dot in (a) and (b) stands for the photodetachment interaction zone. A_n^- in (b) represents the anionic cluster beam. (EZ, Einzel lens; GV, gate valve; TP, turbo pump; CP, cryopump).

the use of virtually any extraction voltages without losing the focusing power.

In this article, the detailed design, simulation, construction, testing, and performance of the new VMI apparatus are reported. In Sec. II, we describe the laser-vaporization cluster source and the time-of-flight (TOF) mass analyzer, as well as the details of the overall VMI system, the electron detection, and the detachment laser. Section III gives the details of the simulations to achieve the optimal VMI lens configuration. Section IV presents the data acquisition and control system, as well as the experimental procedures. Section V reports the detailed characterization of the VMI system and its performance using atomic, cluster, and complex anions. In Sec. VI, a few comments about the different methods for inverse-Abel transformation are given, before some concluding remarks in Sec. VII.

II. APPARATUS DESCRIPTION

Figure 1(a) shows a schematic view of the whole VMI-PES apparatus. It consists of a laser-vaporization supersonic

cluster source, a modified Wiley-McLaren time-of-flight mass analyzer, and the VMI spectrometer. An enlarged view of the latter is given in Fig. 1(b). The cluster source and the TOF mass analyzer are similar to those reported in detail in Ref. 25 and hence only a brief summary is given. Details of the VMI system will be described in this section.

A. The laser-vaporization supersonic cluster source

The laser-vaporization cluster source used in the new VMI apparatus is similar to that used in our magnetic-bottle PES apparatus, described in detail previously.²⁵ Briefly, we focus the second harmonic output (532 nm) of a Nd:YAG laser to a 1 mm diameter spot on a disk target. The detachment laser is operated at 10 Hz and typically 10 mJ pulse energy is used. The path of the vaporization laser beam is collinear with the cluster beam, as shown in Fig. 1(a). Synchronized with the laser vaporization event, two pulsed valves (R.M. Jordan Co., CA) are used to deliver a short and intense helium carrier-gas pulse at a backing pressure of 10 atm. The laser-induced plasma is quenched and cooled by the carrier gas, initiating

nucleation events to form clusters of various sizes and charge states. The nascent clusters are entrained in the carrier gas and undergo a supersonic expansion to produce a cold and collimated cluster beam by a skimmer, 15 cm down stream from the cluster nozzle.

Cold cluster anions are essential for high-resolution PES studies. Negatively charged cluster ions from the laser vaporization source are particularly difficult to cool because of the large heat of formation. Even though active cooling of anions in ion traps has been achieved more recently for PES experiments,^{17,26,27} we have found previously that our “large waiting-room” nozzle can yield fairly cold cluster anions.²⁸ The large waiting-room allows sufficient thermalization of the nascent clusters, while they are further cooled by the subsequent supersonic expansion. The key factor is to allow the clusters sufficient resident time in the large waiting-room nozzle for effective thermalization. Hence, the clusters leaving the nozzle later tend to be much colder, which is controlled by the delay of the ion extraction pulse relative to the vaporization laser pulse. More recently, we have found that a helium carrier gas seeded with 5% Ar can achieve even better cooling effects, manifested by van der Waals complexes of gold cluster anions with Ar.²⁹ Our high-resolution imaging study of Au_2^- achieved a vibrational temperature of ~ 175 K.²⁰ Dimer anions are especially challenging to cool in our laser vaporization source because we cannot achieve long enough resident time in the nozzle due to ion loss. We have recently observed a vibrational temperature of 125 K for AuC_2^- ,²³ whereas for Au_4^- we were able to essentially eliminate all vibrational hot bands by using the helium carrier gas seeded with 5% Ar in combination with an optimal resident time.²¹

B. The time-of-flight mass analyzer

After the skimmer, negatively charged clusters from the collimated beam are extracted perpendicularly into a TOF mass spectrometer (MS) (Fig. 1(a)), which is also similar to that used in our magnetic-bottle PES apparatus.²⁵ Typically a -1 kV high voltage pulse is used for the ion extraction, but higher voltages will be needed to extract heavy clusters. The ion extraction stack can be rotated slightly to achieve better extraction efficiency for heavy clusters. The mass spectrometer involves a modified Wiley-McLaren design, which allows a large ion extraction volume and good mass resolution.^{25,30} The ions are guided by a set of deflectors and focused by two sets of Einzel lenses (EZ1 and EZ2) in the 1.83 m long TOF tube onto a pair of in-line microchannel plate (MCP) detector, placed behind a mass gate and before the entrance to the VMI lens system. The mass resolution ($M/\Delta M$) of the current design is 450 for low masses and it deteriorates somewhat for heavier masses. The in-line MCP ion detector is rotatable and is moved out of the ion path during subsequent VMI experiment (Fig. 1(b)). The mass gate in front of the MCP detector allows only the clusters of interest to enter the VMI lens system. The mass gate is similar to that used in our magnetic-bottle PES apparatus, but without the momentum decelerator.²⁵ Because of the collinear design, ion deceleration is not necessary for the VMI experiment.

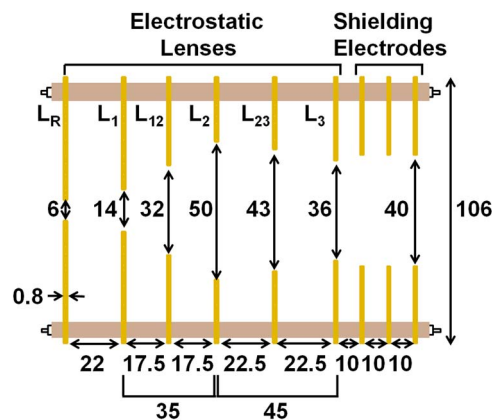


FIG. 2. Details of the optimized VMI lens assembly. All units are in mm.

Figure 1(b) shows an expanded view of the VMI spectrometer, where the mass gate, a set of aperture lens (EZ3), and the in-line MCP ion detector can be seen more clearly. The selected clusters are refocused by an aperture lens system (EZ3) right after the mass gate and pass through a so-called reference tube before entering the VMI lens system (Fig. 1(b)). The purpose of the reference tube is to prepare the clusters to go through the repeller plate of the VMI lens without being defocused. The reference tube is at ground potential when the selected ions enter it, but it is switched to the same voltage as the repeller plate (L_R in Fig. 2) of the VMI lens once the clusters are inside the reference tube. However, in practice we find that the re-referencing of the ions to the repeller voltage is not necessary because the kinetic energies of the ions are significantly larger in comparison to the voltage applied to the repeller plate. No significant loss of ion intensity is observed while the reference tube is simply grounded. However, if the VMI repeller voltage is large for photoelectrons with high kinetic energies, then the re-referencing is critical to optimize the transmission of the cluster anions into the photodetachment interaction zone.

C. The velocity-map imaging lens and the electron detection system

Figure 2 shows the detailed configuration of our VMI lens system, which is based on the multilens design by Suits and co-workers for slicing imaging of ions,²⁴ and modified and optimized for high resolution photoelectron imaging. It consists of a three-electrode VMI scheme with more careful field shaping and shielding to achieve optimal focusing. The optimization and operation of the VMI spectrometer will be presented in Sec. III. The dimensions given in Fig. 2 (all in mm) correspond to the optimized configuration. All the electrodes, including the shielding electrodes, are made of oxygen-free copper and gold-plated. The thickness of the electrodes is 0.8 mm and their outer diameter is 106 mm. The distances indicated between the electrodes are measured from the center of each electrode. As shown in Fig. 2, the following notation is used: L_R and V_R stand for the repeller electrode and its voltage, respectively. L_1 , L_2 , and L_3 represent the three active electrodes, whereas L_{12} and L_{23} are guarding electrodes

between L_1 - L_2 and L_2 - L_3 , respectively, to prevent fringe field effects. The voltages applied to L_1 and L_2 are designated as V_1 and V_2 , respectively, whereas L_3 and the shielding electrodes are all grounded.

The selected clusters enter the VMI lens system through a 6 mm diameter aperture on the repeller plate (L_R) and are crossed by the detachment laser beam in the interaction zone, defined as the center between electrodes L_R and L_1 (shown by the red dot in Fig. 1). The photodetached electrons are accelerated toward a position-sensitive detector consisting of a set of 75 mm diameter MCP coupled to a P47 phosphor screen (Photonis USA, Inc) and a charge-coupled device (CCD) camera (Uniq Vision Inc., Model UP930CL, 1024×1024 pixels). The imaging detector is located at the end of the VMI spectrometer and 50 cm away from the interaction region (Fig. 1). The VMI lens and the entire electron flight path are enclosed within two concentric cylinders of μ -metal shielding (0.51 mm thick, 14.1 and 17.7 cm diameter, respectively). There are two holes (2 cm diameter) on the μ -metal shielding below and above the interaction zone for the detachment laser beam.

The VMI system is housed in a 12 in. cubic stainless steel vacuum chamber, evacuated by a cryopump (CTI-Cryogenics) to achieve ultra high vacuum. The detachment laser beam enters the interaction zone via a 20 in. long (1.5 in. diameter) stainless steel nipple extended from the bottom of the vacuum chamber and exits the interaction zone via another 20 in. long (1.5 in. diameter) nipple on the top of the vacuum chamber (not shown in Fig. 1). An MgF_2 window is mounted at the Brewster angle at the end of each nipple to allow transmission of the detachment laser beam in and out of the vacuum chamber. The interior of the nipples is painted with Aquadag to reduce light scattering and photoelectric effects. A 1 cm diameter aperture is mounted inside each nipple for laser beam collimation.

A National Instrument (NI) PXI-mainframe system is used to control the whole apparatus and for data acquisition (see Sec. IV below). Photoelectron images are usually averaged with 50 000–200 000 laser shots. The images are usually quite round and there is no need for post-imaging circularization treatment. However, for low electron extraction voltages ($|V_R| < 150$ V), quadrant-symmetrization is needed. The raw or quadrant-symmetrized images are then inverse-Abel transformed to obtain the three-dimensional (3D) electron distributions. We usually perform the reconstruction using either the BASEX³¹ or pBASEX³² programs, which yield similar results, as will be discussed in Sec. VI.

D. The detachment laser system

To perform high-resolution VMI experiments in the SEVI mode, a tunable detachment laser system is essential. Our new VMI apparatus is equipped with a Continuum Sunlite EX OPO system (445–1750 nm, line width <0.075 cm^{-1} and pulse width of 3–6 ns) pumped by an injection-seeded (SI-2000) Continuum Powerlite laser (Powerlite DLS 9020, repetition rate of 20 Hz, 1.8 J/pulse at 1064 nm, 5–9 ns pulse width, 1 cm^{-1} line width unseeded, and 0.003 cm^{-1} line

width seeded). A Sunlite FX-1 frequency-doubling module extends the available wavelengths in the 225.5–450 nm range (<0.3 cm^{-1} line width and a pulse width of 3–6 ns). A half-wave plate combined with a high-quality Glan-Laser polarizer is used to achieve a high degree of polarization parallel to the imaging detector plane.

III. OPTIMIZATION OF THE VMI CONFIGURATION FOR HIGH-RESOLUTION PHOTOELECTRON IMAGING

The final high-resolution VMI lens configuration was accomplished by simulations using the 3D ion trajectory package, SIMION 8.0.³³ The main idea was based on the multi-lens velocity-mapping design for “direct current slice imaging” of photoions, reported by Suits and co-workers.²⁴ The final electrode configuration and dimensions are as given in Fig. 2.

In the initial simulation, no shielding electrodes or the guarding electrodes L_{12} and L_{23} were used. The purpose of the guarding electrodes added later is to avoid fringe field penetration due to the large distances between L_1 - L_2 and L_2 - L_3 . To mimic the photoemission events in the interaction zone, we created 100 electrons in each SIMION run and distributed them in a cylinder of 3 mm diameter and 2 mm height, with a given initial kinetic energy to produce a spherical expansion. We employed a kinetic energy of 0.5 eV for the initial simulations and verified that the focusing conditions remained the same for different electron kinetic energies. The voltage (V_R) of the repeller (L_R) was chosen as -600 V for the initial simulations. The variables to be optimized in the simulations were numerous: the distance (d_{R-1}) between the repeller (L_R) and the first electrode (L_1); the distance (d_{1-2}) between the electrodes L_1 and L_2 ; the distance (d_{2-3}) between the electrodes L_2 and L_3 ; the size of the aperture for each electrode (Y_R , Y_1 , Y_2 , and Y_3). More importantly, the voltages on the first and second electrodes (V_1 and V_2) were scanned for each geometrical configuration of the whole assembly, while keeping V_R at -600 V and V_3 at ground potential.

All of these variables to be optimized in the simulations would generate an enormous number of possible combinations at a given step size for each variable. A script was written in SIMION to generate a different geometry, vary the V_1 and V_2 voltages at a determined step (usually 1 V per step), and register the dispersion (or spot size) of the electrons on the detector. With SIMION 8.0, it is possible to run parallel simulations in the same computer, as long as there is sufficient memory. Thus, six SIMION .lua scripts were run at the same time in two personal computers (with 16G RAM each). First, some arbitrary sizes for the electrode apertures were chosen, while varying only the distances between the electrodes at relatively large steps (2–3 mm per step). The same procedure was employed by varying the sizes of the apertures and keeping the distances between the electrodes at some arbitrary values. The results were analyzed to yield the most promising geometrical configuration of the whole assembly. Subsequently, the procedure was repeated by varying the electrode distances at smaller steps (1 mm per step) while keeping the best electrode aperture sizes obtained in the previous step. The same was done by varying the sizes of the electrode apertures. The

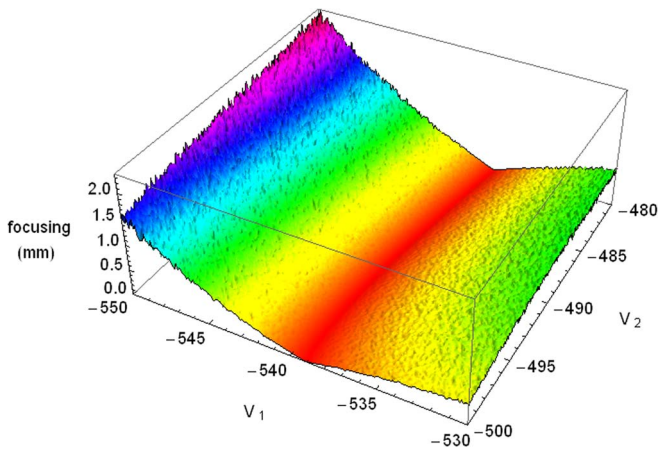


FIG. 3. Results of SIMION simulations about the dispersions or focusing spot sizes in mm for electrons, versus the voltages, V_1 and V_2 in volt, applied to the L_1 and L_2 electrodes, respectively (see Fig. 2). $V_R = -600$ V and $V_3 = 0$ V.

process was repeated until an optimal configuration was found under a pre-set criterion of focusing. Then, the voltages (V_1 and V_2) were also varied at smaller steps. The whole procedure was repeated once again until the best configuration was finally achieved. In the last step, we also added the shielding electrodes in the simulation (Fig. 2).

To save time, we did the simulations initially using 2D geometries and applied cylindrical symmetry. The 3D geometry for the best configuration was further verified. During each simulation, the geometries, voltages, and the focusing (in mm) were stored in a file. A Mathematica³⁴ program was written to help analyze the enormous amount of data. Figure 3 displays the dispersion of the electrons for the final configuration by varying V_1 and V_2 around the optimal V_1/V_2 ratio. It illustrates the complexity of the simulations and the complicated parameter landscape. Figure 3 shows that for each V_2 setting there is a V_1 value that gives the best focusing condition. Additionally, there are multiple local minima, which can complicate locating the global minimum during the simulations. The simulation was taken as finished once we reached a focusing of $3 \mu\text{m}$, which represents sub-pixel resolution (each pixel of the camera corresponds to approximately $72 \mu\text{m}$ in the detector). The $3 \mu\text{m}$ focusing size is in fact even smaller than the size of a MCP grid ($10 \mu\text{m}$ channel diameter + $2 \mu\text{m}$ for the gap between two microchannels). This tight focusing is certainly not representative as it corresponds to the best conditions (for a given electron kinetic energy); for other kinetic energies the focusing conditions may be slightly off (but still at sub-pixel resolution). In any case, for our experimental kinetic energy range, the focusing of the electrons was always below $40 \mu\text{m}$, still at sub-pixel resolution. In fact, the worst focusing condition was never larger than $70 \mu\text{m}$ at any conditions, i.e., independent of the repeller voltages applied (from -100 V to -2000 V) and independent of the kinetic energies of the photoelectrons. Thus, the upper limit (or the worst case scenario) of our focusing condition is approximately $70 \mu\text{m}$, which corresponds to a velocity resolution ($\Delta v/v$) of 0.18% and a kinetic energy resolution ($\Delta KE/KE$) of 0.36%. This resolu-

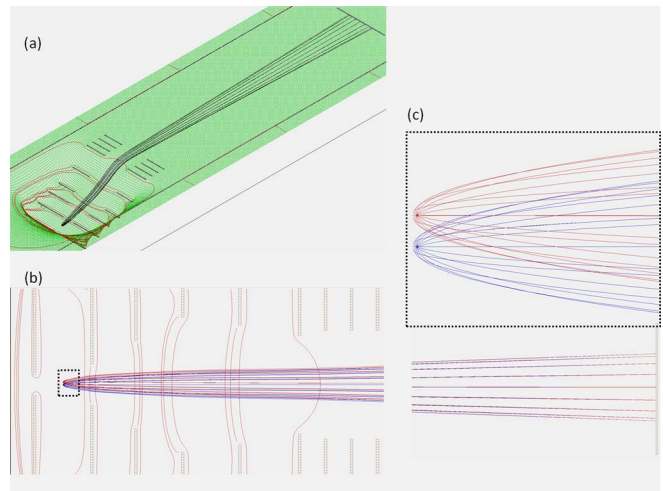


FIG. 4. Equipotential surfaces of the optimized VMI lens configuration and selected electron trajectories. Panel (a) shows the total view, while (b) and (c) are zoomed in to show the details. Electrons emitted in the same angle but different start positions (b) arrive at the same point on the detector plane (c).

tion is similar to that described in Ref. 15, but with a considerably larger interaction region between the cluster beam and the laser beam in the current case (3 mm diameter and 2 mm height).

In our first design, there were no guarding electrodes, L_{12} and L_{23} (Fig. 2). As shown in Fig. 2, it may be suspected that the large gaps of 35 and 45 mm between the L_1 - L_2 and L_2 - L_3 electrodes may cause fringe-field problems. Indeed, after we installed the electrodes and took some preliminary photoelectron images, we found that, although the focusing was good, the images appeared slightly distorted due to the penetration of the fringe field. The problem was readily solved by adding the guarding electrodes L_{12} and L_{13} with aperture sizes and voltages corresponding to the average of the neighboring electrodes. We re-ran the simulations to reach the final configuration given in detail in Fig. 2.

Figure 4(a) shows a schematic diagram of the imaging lens and equipotential surfaces with the electron trajectories for the final VMI configuration. Figure 4(b) shows the basics of velocity-map imaging and how electrons originated at different positions (red and blue) but with the same initial ejection angle and energy are mapped to the same point of the detector (Figure 4(c)), as first demonstrated in Ref. 4.

Although our interest was on photoelectron imaging, we also did simulations for ion imaging, similar to that reported by Suits and co-workers.²⁴ We found that the current three-electrode configuration gives similar stretching of the ion cloud as in Ref. 24, but with only half of the TOF distance. Thus, our electrode configuration can also be advantageous for ion imaging.

IV. THE DATA ACQUISITION SYSTEM AND EXPERIMENTAL PROCEDURES

The data acquisition system is based on the PXI platform from National Instruments. The control of the whole appa-

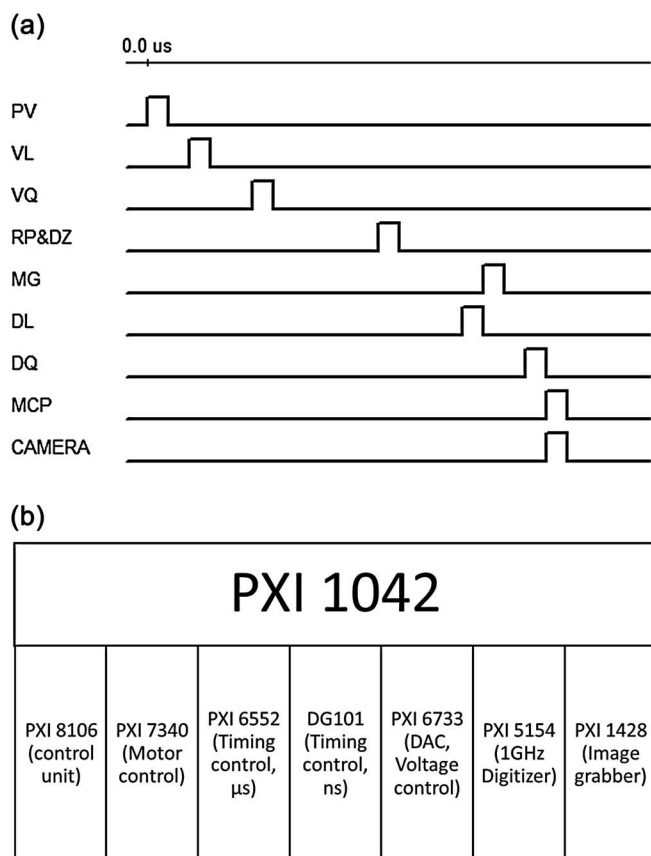


FIG. 5. (a) Timing sequence for one experimental cycle. PV: pulsed valve; VL: vaporization laser flash lamp; VQ: vaporization laser Q-switch; RP: TOF-MS repeller; DZ: TOF-MS digitizer; MG: mass gate; DL: detachment laser flash lamp; DQ: detachment laser Q-switch. PV, VL, VQ, RP, DZ, and MG work at 10 Hz; DL, DQ, MCP, and CAMERA work at 20 Hz. (b) The PXI chassis and the major control modules of the data acquisition system. See text for detailed functional descriptions.

ratus is divided into three main tasks: timing control, voltage control, and data acquisition. A flow diagram of the timing of the experiment for one experimental cycle is illustrated in Fig. 5(a). The timing control involves synchronization of the pulsed valves (PV) to deliver the carrier gas, the vaporization laser/vaporization laser Q-switch (VL/VQ), the stepping motors, high voltage switches, the detachment laser, the digitizer for mass spectra, and the CCD camera. The voltage control refers to adjusting the horizontal and vertical ion deflectors in the TOF-MS (Fig. 1(a)). Finally the data acquisition includes taking TOF mass spectra and grabbing photoelectron images from the camera. It should be noted that clusters are produced with a repetition rate of 10 Hz, whereas the detachment laser and image acquisition operate at 20 Hz with the clusters off at alternate laser shots for the purpose of background subtraction.

All the major control modules are embedded in a PXI-1042 Chassis, as schematically shown in Fig. 5(b). The heart of the control hardware is the PXI 8106 module, which is basically a PC unit integrated with peripheral I/O ports, running under Microsoft Windows. The PXI 6552 module is a 100 MHz digital waveform generator/analyzer with μs resolution and is used to generate the main timing sequence. The DG101 module (Mink Hollow Systems, Inc.), a four-

channel digital delay generator, generates timing signals with nanosecond accuracy. The PXI 7340 module controls two stepping motors for the movement of the target, one for rotation and the other one for up-and-down translation. The target rotates in a constant linear speed so that the target surface is ablated uniformly. The PXI 6733 module is used to control the voltages (-10 V to 10 V) of the two pairs of ion deflectors. The PXI 6733 voltage signals are amplified by a factor of 50 to provide the real deflector voltages in the range from -500 V to 500 V . The PXI 5154 module is a 1 GS/s digitizer used to acquire TOF mass spectra. The sampling rate of the digitizer can be set at 100, 200, or 500 MHz, depending on the requirement of the experiment. Finally, the image acquisition is performed by the PXI 1428 frame grabber connected via a camera link to a Uniq UP930CL B/W digital CCD camera. The camera has a 1024×1024 pixels with a 1/2 in. CCD sensor. It works at a repetition rate of 20 Hz to acquire both imaging signals and background noise at alternate detachment laser shots.

All the timings, voltages, the movement of the target, camera setup, and data acquisition are controlled by the computer. The timing and voltages can be scanned to optimize experimental conditions. The experimental timing is controlled in three levels, starting from the control program to PXI 6552 to DG101. The trigger pulses involving cluster production (PV, VL, VQ, and RP in Fig. 5(a)) are all generated by the PXI 6552 module with an accuracy of $0.5\ \mu\text{s}$. During each experimental cycle, two timing sequences (one for the signal and the other for the background) are created and written into the PXI 6552 onboard memory. These two pre-written timing sequences are “played” in turn every 50 ms to generate the whole timing sequence for one experimental cycle. The timings for the mass gate, the detachment laser, and the imaging MCP are generated by the DG101 module with a 1 ns accuracy, triggered by a signal from the PXI 6552. Photoelectron images are processed *in situ*. The center of mass of each electron image captured by the camera is calculated and recorded, using the sub-pixel centroiding technique.^{35–37} The accumulated image is monitored and saved together with the experimental parameters.

V. PERFORMANCE

A. The image quality and image calibration

One of the important and challenging issues for high-resolution imaging is to achieve perfectly circular images. Any imperfection in the roundness of the image will significantly affect the resolution. Although there are different tricks to correct image distortions, such as radial circularization or quadrant symmetrization, our optimized VMI configuration can achieve images, which do not require post-imaging corrections prior to inverse-Abel transformation. As mentioned above, our initial design did not include the guarding electrodes (L_{12} and L_{23} in Fig. 2), which resulted in image distortions due to fringe field penetration. Furthermore, images for electrons with different kinetic energies were not concentric and their centers could be off by one or two pixels. After the introduction of the L_{12} and L_{23} guarding electrodes, we

can achieve almost perfectly round and concentric images for electrons with different kinetic energies. For images with a radius of 420 pixels, we can achieve a roundness of only one pixel difference between the longest and shortest radii, i.e., a non-circularity of only about 1.0025. Images of this quality do not need circularization treatment prior to inverse-Abel transformation.

If we assume the interaction zone as a point source, the relation between the image radius (R), the image expansion speed or the interested photoelectron velocity (v), and the time-of-flight (t) of the photoelectrons from the interaction zone to the imaging detector are given simply by

$$R = vt. \quad (1)$$

Hence, the kinetic energy of the photoelectron is related to R , according to

$$\text{KE} = 1/2mv^2 = 1/2m(R^2/t^2) \quad (2)$$

or

$$\text{KE} = aR^2, \quad (3)$$

where m is the mass of the electron and a is simply a constant depending on the geometry of the VMI spectrometer and the repeller voltage (V_R). The constant a can be readily determined by taking PE images of known atomic anions (usually Au^- or Bi^-) at different photon energies to cover the whole area of the detector. We have found that if the position of the detachment laser focus is set in the middle of the repeller (L_R) and extractor (L_1) plates, the calibration constant a is barely changed from day-to-day operation, yielding sub-meV accuracies for photoelectron kinetic energies via Eq. (3) for small R or low energy electrons.^{20–23} Furthermore, the calibration parameter a increases essentially linearly with the voltage applied to the repeller plate (V_R). With our current geometry (a 50 cm distance between the interaction zone and the imaging detector plane), the constant a is 3.720×10^{-6} for $V_R = -300$ V, and for KE in eV and R in μm . The linearity between a and V_R is true even for low repeller voltages, although the images exhibit more distortions at very low $|V_R|$. Thus, for our current VMI configuration, Eq. (3) becomes

$$\text{KE} = 3.720 \times 10^{-6} (|V_R|/300) R^2, \quad (4)$$

where KE is in eV, V_R in V, and R in μm . This equation is usually fairly accurate for our current VMI configuration and gives accuracies of the order of meV for quick conversions of images to energies. However, calibrations must be done carefully and independently for each measurement for sub-meV accuracy.

The optimal voltage ratios obtained from our simulations for the electrodes under our current VMI configuration are the following: $V_1/V_R = 0.89$, $V_2/V_R = 0.80$ [$V_{12} = (V_1 + V_2)/2$; $V_{23} = (V_2 + V_3)/2$; $V_3 = 0$ V]. The real experimental voltage ratios applied to the electrodes are lower than those from the simulations for optimal resolution. Because of expected mechanical imperfections of the VMI assembly including alignments, careful fine-tuning is necessary to achieve the best possible resolution if V_R is changed.

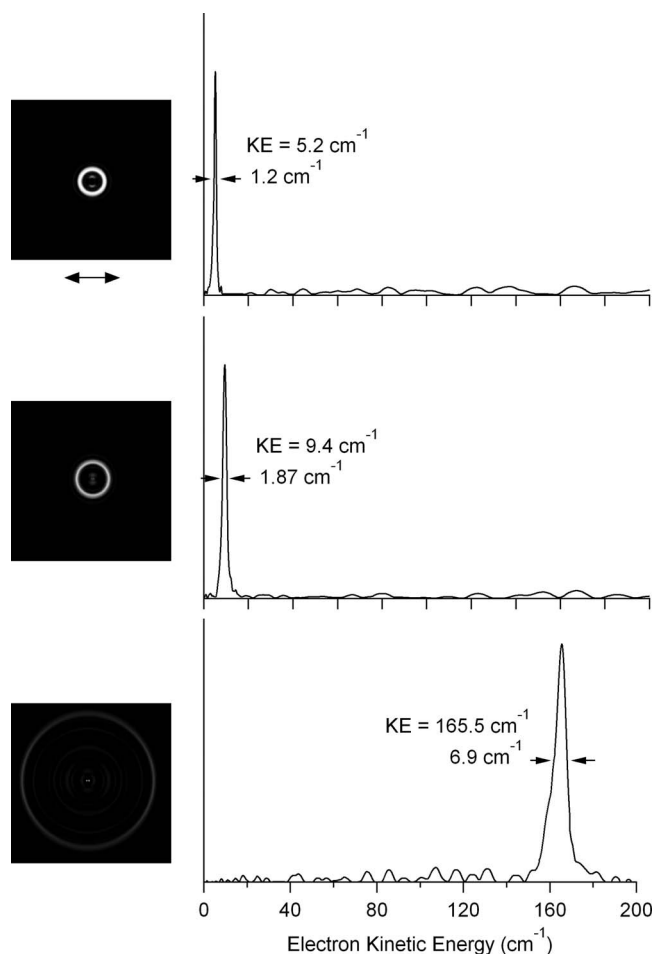


FIG. 6. Photoelectron images and spectra of Bi^- at kinetic energies of 165.5, 9.4, and 5.2 cm^{-1} obtained after the inverse-Abel transformation. The detachment wavelengths used were 521.24, 525.51, and 525.63 nm, respectively. The double arrow indicates the laser polarization. The repeller voltage (V_R) was at -100 V.

B. The resolution of the new VMI system tested with atomic anions

The new VMI apparatus has been tested extensively using photoelectron images of Bi^- . We will also present some results of Au_2^- and a complex organic anion ($\text{C}_6\text{H}_5\text{O}^-$) to show that the same level of performance is also attainable for molecular systems. The potentials and capabilities of the new VMI system have been demonstrated in several initial studies on size-selected clusters, i.e., Au_2^- , Au_4^- , and AuC_2^- .^{20–23}

Figure 6 shows the photoelectron images of Bi^- after inverse-Abel transformation together with the corresponding angular-integrated PE spectra in kinetic energies measured at laser wavelengths of 5.2, 9.4, and 165.5 cm^{-1} above the detachment threshold. The ground state of Bi^- is $^3\text{P}_2$ ($6p^4$) and the electron affinity (EA) of Bi is accurately known (0.94236 eV),³⁸ corresponding to the transition, $\text{Bi} (6p^3\ ^4\text{S}_{3/2}) \leftarrow \text{Bi}^- (6p^4\ ^3\text{P}_2)$. The Bi^- anion provides a convenient calibrant because of its favorable detachment cross sections near threshold according to the Wigner threshold law³⁹ and its multiple detachment transitions just above the threshold.⁴⁰ The spectra shown in Fig. 6 correspond to the $\text{Bi} \ ^2\text{D}_{3/2} \leftarrow \text{Bi}^- \ ^3\text{P}_2$ transition with an electron binding energy of 2.35814 eV. The

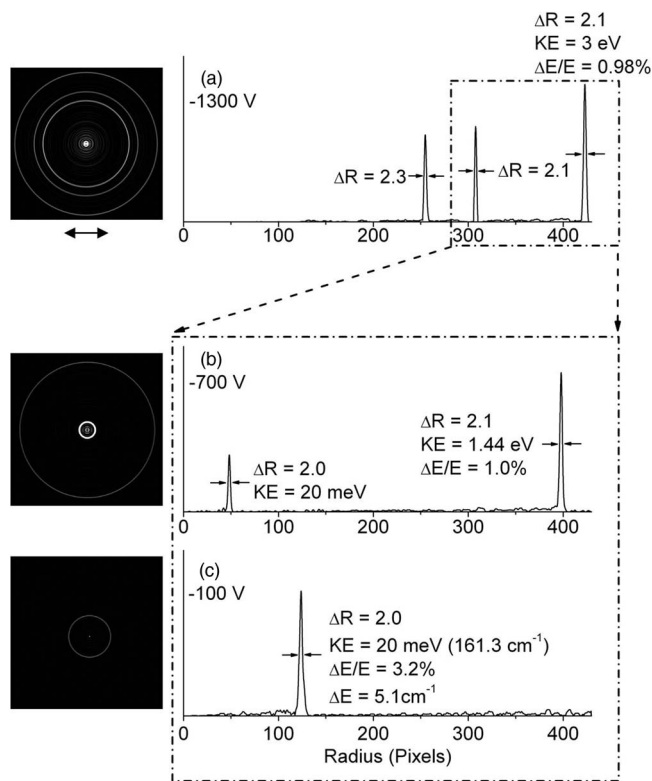


FIG. 7. Photoelectron spectra of Bi^- in radius at detachment energies of (a) 3.9300 eV, and (b) and (c) 2.3781 eV, together with the photoelectron images after inverse-Abel transformation. The repeller voltages are $V_R = -1300, -700,$ and -100 V, as given in each spectrum. The double arrow in (a) indicates the laser polarization.

1.2 cm $^{-1}$ line width (FWHM) for the near threshold detachment represents the best resolution that has been achieved to date for a VMI system. The relative resolution ($\Delta KE/KE$) improves as the kinetic energy is increased, achieving a line width of 6.9 cm $^{-1}$ for 165.0 cm $^{-1}$ electrons. The spectra shown in Fig. 6 were taken with $V_R = -100$ V.

To test the focusing capability of our new VMI system, we took photoelectron images of Bi^- at different repeller voltages (V_R) and using different detachment wavelengths accordingly, as shown in Fig. 7. The images after the inverse-Abel transformation are shown in the left panels, whereas the converted spectra are plotted in the scale of pixels or image radius. Figure 7(a) shows the image and converted PE spectrum of Bi^- at a detachment energy of 3.9300 eV and $V_R = -1300$ V. The peaks correspond to detachment transitions from the Bi^- 3P_2 ground state to the $^4S_{3/2}$, $^2D_{3/2}$, and $^2D_{5/2}$ states of Bi with electron binding energies of 0.94236, 2.35814, and 2.85637 eV, respectively.^{38,40} As shown in Fig. 7, all the peaks have a width (FWHM) of approximately 2 pixels, indicating the importance of sub-pixel centroiding.³⁵⁻³⁷ It is significant to note that decreasing the magnitude of the repeller voltage does not affect the focusing conditions of our VMI lens, as seen in Figs. 7(b) and 7(c) taken at a detachment energy of 2.3781 eV. The peak width stays at 2 pixels, regardless of the magnitudes of V_R . However, for $|V_R|$ below 150 V the images start to show distortions and the circularity of the images is slightly compromised. Consequently, the photoelectron

image used to obtain Fig. 7(c) has been quadrant-symmetrized before the inverse-Abel transformation.

However, a lower repeller voltage can improve the energy resolution for low energy electrons. This can be seen if we differentiate Eq. (3) to obtain the following relationship between ΔKE and ΔR :

$$\Delta KE/KE = 2(\Delta R/R). \quad (5)$$

A lower magnitude of the repeller voltage gives a larger radius for the PE images. Inasmuch as the focusing is maintained, Eq. (5) suggests that the resolution in the energy scale is increased. Fig. 7(c) gives a peak width of 5.1 cm $^{-1}$ for the Bi^- $^2D_{3/2} \leftarrow \text{Bi}^-$ 3P_2 transition with a kinetic energy of 161.3 cm $^{-1}$ at $V_R = -100$ V. In principle, the lower the repeller voltage, the better the resolution for slow electrons. However, the -100 V repeller voltage is a practical limit for our current design because image distortions become severe for $|V_R| < 100$ V. A -300 V repeller voltage provides a good compromise in our usual operation. At $V_R = -300$ V, our current configuration allows detection of electrons up to 0.75 eV kinetic energy with the 50 cm electron flight path and the 75 mm diameter imaging detector. To image electrons with higher kinetic energies, higher magnitudes of the repeller voltages are necessary.

C. Performance of the new VMI system tested with cluster anions

We have demonstrated the capabilities of our new VMI apparatus for a number of cluster systems.²⁰⁻²³ The first cluster that we studied using the new VMI apparatus was Au_2^- , for which we obtained completely vibrationally resolved spectra for the transition from the ground electronic state of Au_2^- ($^2\Sigma_u^+$) to that of Au_2^- ($^1\Sigma_g^+$). We reported the narrowest line width of 2.8 cm $^{-1}$ from VMI of a molecular system for electrons with 11.2 cm $^{-1}$ kinetic energy.²⁰ The previous narrowest line width for a molecular system was 4.1 cm $^{-1}$ for 13 cm $^{-1}$ electrons for C_5^- cooled in a cryogenic ion trap.¹⁷ The Au_2^- dimer anion is a good cluster system to test our new VMI apparatus because of the numerous vibrational lines available for the ground state detachment transition.⁴¹ We re-measured some of the spectra at $V_R = -100$ V and compared them with those reported in Ref. 20, which were measured at $V_R = -300$ V. The results are given in Fig. 8, where the inset in each spectrum at a given wavelength represents the new data at $V_R = -100$ V. In each case, the resolution is improved in the new measurement relative to the published results,²⁰ consistent with Eq. (5). For example, Fig. 8(c) displays the spectrum at 590.41 nm; the peak widths corresponding to the $KE = 133$ and 323 cm $^{-1}$ peaks are 10.5 and 15.8 cm $^{-1}$ at $V_R = -300$ V, respectively, but they become 6.5 and 9.4 cm $^{-1}$ at $V_R = -100$ V (inset in Fig. 8(c)). Similarly, Figs. 8(a) and 8(b) show the PE spectra taken at 619.92 and 604.80 nm, respectively. The same level of improvement is observed for the data taken at $V_R = -100$ V, relative to those at $V_R = -300$ V. Specifically, the peak at $KE = 124.8$ cm $^{-1}$ in the 619.92 nm (Fig. 8(a)) has a width of 8.1 cm $^{-1}$ at $V_R = -300$ V, but it becomes 6.1 cm $^{-1}$ at V_R

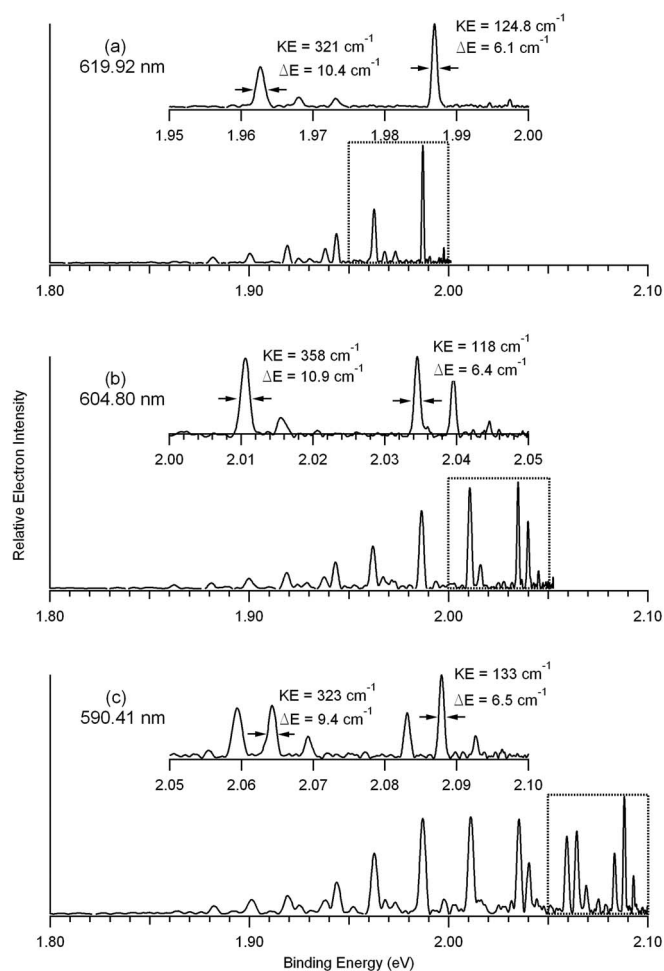


FIG. 8. Comparison of the photoelectron spectra of Au₂⁻ at different detachment photon energies: (a) 619.92 nm (2.0000 eV), (b) 604.80 nm (2.0500 eV), and (c) 590.41 nm (2.1000 eV) and at two repeller voltages, -300 V and -100 V. The spectra at V_R = -300 V are from Ref. 20. The inset in each case represents the spectrum re-measured at V_R = -100 V. The kinetic energy and the corresponding peak width (FWHM) for some of the peaks are given in the V_R = -100 V spectra.

= -100 V (inset in Fig. 8(a)). Even though the images are slightly distorted at V_R = -100 V, we still achieve better resolution according to Eq. (5), because of the superior focusing power of our VMI design.

The current VMI design not only provides cm⁻¹ (or sub-meV) resolution for very low energy photoelectrons, but also yields very good resolution for higher energy electrons up to 3 eV (Fig. 7(a)). We can achieve an energy resolution of less than 0.53% by using the appropriate repeller voltages and the sub-pixel centroiding method.^{35–37} This performance for high kinetic energy electrons is comparable to that reported in Ref. 15, which offers heretofore the best relative energy resolution for higher kinetic energies ($\Delta KE/KE = 0.38\%$ for KE = 0.87 eV). The current design maintains the same level of focusing for |V_R| > 300 V. For example, images taken at -1300 V are almost perfectly round; and sub-pixel focusing is attainable for electrons with a wide range of kinetic energies (Fig. 7). Overall, we conclude that the current VMI design provides the best performance with a wide energy range from near threshold electrons to electrons with several eV of kinetic energies.

D. Performance of the new VMI system tested with complex anions from electrospray

The new VMI lens system has been adapted to our electrospray-PES apparatus⁴² with a cryogenic ion trap.^{26,43} It has yielded rotational profiles in PE images and spectra of complex organic anions^{44,45} and has allowed completely vibrationally resolved PE spectra to be obtained for cold C₆₀⁻ very recently.⁴⁶ The latter probably represents the most complex anions to have been investigated by PE imaging to date.

Figure 9 shows the PE images and spectra of the phenoxide anion (C₆H₅O⁻) cooled to 20 K in a cryogenic ion trap at four detachment wavelengths. Details of these data have been published and explained previously.⁴⁴ All the peaks correspond to vibrational excitations of the phenoxy neutral radical (C₆H₅O[•]) ground state. The cold anion eliminates all vibrational hot bands, compared to a previous SEVI study.⁴⁷ In addition, the good signal-to-noise ratios in the current work allowed vibrational modes with very weak Franck-Condon factors to be observed. The line width of all the peaks, in particular those near threshold, are all significantly broader than the instrumental resolution, due to rotational broadening, as shown in the inset of Fig. 9(a), where the fine features of the

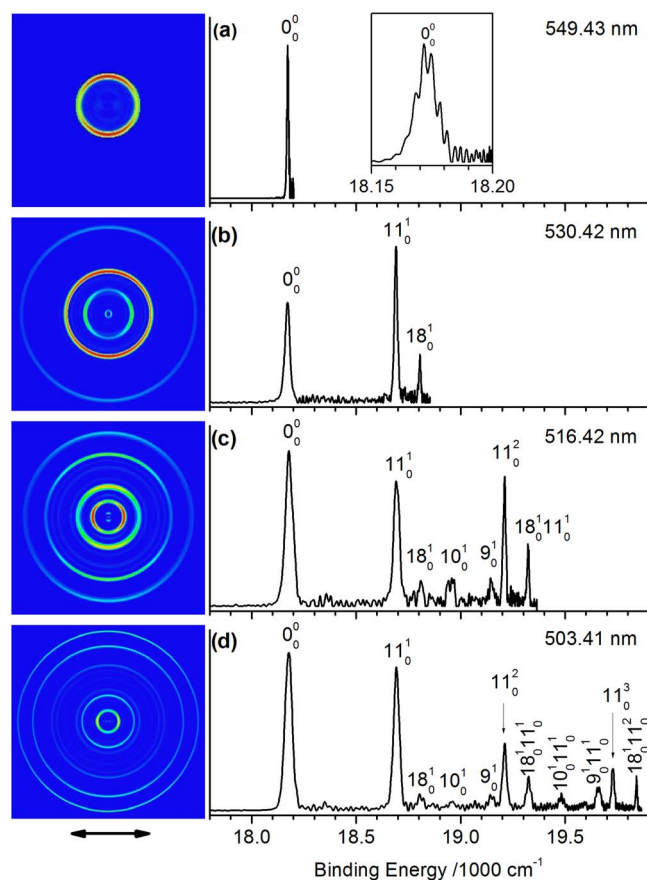


FIG. 9. Photoelectron imaging of phenoxide (C₆H₅O⁻) cooled to 20 K: (a) at 549.43 nm (18 200.8 cm⁻¹); (b) at 530.42 nm (18 853.1 cm⁻¹); (c) at 516.42 nm (19 364.2 cm⁻¹); and (d) at 503.41 nm (19 864.7 cm⁻¹). The photoelectron images after inverse-Abel transformation are shown on the left. The laser polarization is given by the double arrow below the images. The images are calibrated by the known spectra of Au⁻. The observed vibrational structures are labeled according to the vibrational modes of phenoxy. From Ref. 44.

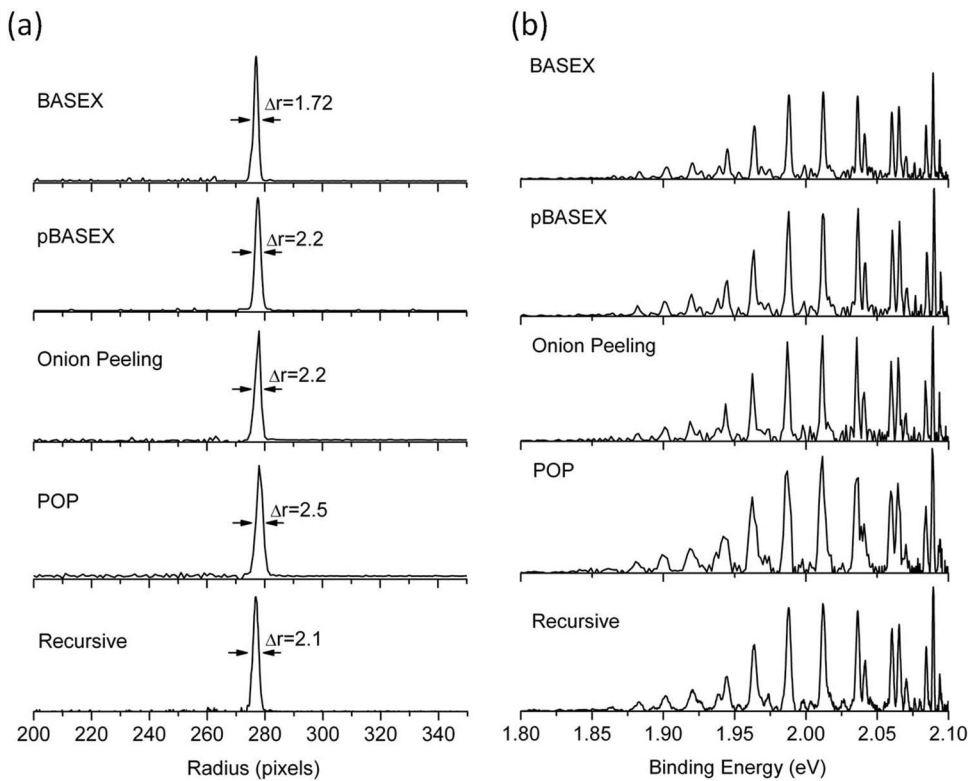


FIG. 10. Comparison of different inversion methods for (a) Au^- taken at 413.28 nm (3.0000 eV) and $V_R = -700$ V and for (b) Au_2^- taken at 590.41 nm (2.1000 eV) and $V_R = -300$ V.

0_0^0 vibrational peak should be due to unresolved rotational excitations. In another study on deprotonated uracil anion,⁴⁵ we have shown that the rotational temperatures can be as high as 35 K when the ion trap is operated at 4.4 K. The spectra shown in Fig. 9 were taken at an ion trap temperature of 20 K,⁴⁴ and the rotational temperature of the phenoxide anions was expected to be much higher than 35 K. Hence, rotational cooling will become a significant issue for high resolution PE imaging of complex anions.

VI. COMPARISON OF THE DIFFERENT INVERSION METHODS

Most of the commonly used inversion algorithms for the inverse-Abel transformation have been carefully studied previously for ion imaging.⁴⁸ Here we briefly compare the different methods for PE imaging. Figure 10(a) shows the inverted spectrum of Au^- in radius taken at a photon energy of 3.0000 eV using the BASEX,³¹ pBASEX,³² Onion Peeling,⁴⁹ and Polar Onion Peeling (POP)⁵⁰ methods. The recursive method was done using the procedure described by Hansen and Law⁵¹ with a homemade program written with Mathematica.³⁴ Overall there is no appreciable difference, other than the fact that the BASEX and the recursive methods offer the possibility of selecting the step size when calculating the velocity distribution and hence can yield sharper features in principle. Additionally, the pBASEX method usually gives smoother features by default, but at the cost of losing resolution due to the size of the Gaussian functions used. The default number of radial functions results in a Gaussian shape extending over

2 pixels. Changing the default to $\text{NR} = 1024$, $\text{NK} = 512$, and $\sigma = 1$ in the pBASEX code³² produces the image shown in Figure 10(a) and the resolution is enhanced and comparable to the other methods. Figure 10(b) displays the results for Au_2^- taken at a photon energy of 2.1000 eV, showing again that the differences among the different inversion methods are minimal.

It should be pointed out that all the inversion codes are limited to images with 1024×1024 pixels (or 1280×1280 pixels for the Onion Peeling program), which is a major drawback nowadays that sub-pixel focusing is achievable. It is becoming common that one needs to either use a higher resolution camera or to bin an image into a larger pixel number. Hence there seems to be room to improve these codes as high-resolution VMI designs are achieved. The pBASEX method on the other hand can be easily modified to set larger basis sets on bigger images and has no limitations (other than the amount of RAM memory that will be used). Finally, the recursive method proposed in Ref. 51 is quite good as it is very straightforward to implement and it allows the inversion of any sized image without any large memory requirement. In fact, we found that the method offers a good quality inversion even without the smoothing or Kalman filtering, except for extremely noisy images.

In summary, all the available codes provide a good quality inversion, although we agree with Ref. 48 that BASEX performs slightly better than the other codes. In particular, because it also accounts for sharper features, it is usually our preferred method. The method described in Ref. 51 is also excellent with the only drawback that it is relatively time

consuming. Since it can invert images larger than 1024×1024 pixels, it can be used together with BA-SEX. The pBASEX method is also one of our preferred methods due to its simplicity and its superior performance to handle noisy images. We have found that this is particularly useful for PE spectra at high photon energies. The Onion Peeling method has a very useful way of calculating the anisotropy parameter by selecting a peak in the velocity distribution. The POP method has the great advantage that the program is written in LabVIEW and hence it is very easy to implement directly in our image acquisition software.

VII. CONCLUSIONS

We report the details of the design, construction, testing, and performance of a new VMI apparatus for high-resolution photoelectron spectroscopy of size-selected anion clusters. The apparatus couples an optimized multilens VMI spectrometer with a laser vaporization supersonic cluster source and a time-of-flight mass analyzer. The new VMI design is based on a three-electrode configuration and can achieve an electron kinetic energy resolution of $\Delta KE/KE = 0.53\%$ for high energy electrons and sub-meV resolution for near threshold electrons. The testing and performance of the new apparatus were done using atomic anions, cluster anions, and complex organic anions. The 1.2 cm^{-1} line width achieved for Bi^- represents the best resolution for atomic systems while the 2.8 cm^{-1} line width observed for Au_2^- represents the best resolution for a molecular system from VMI. It is shown that high resolution VMI of anions can yield important vibrational information for neutral clusters and molecules, which will be complementary to infrared spectroscopy.

ACKNOWLEDGMENTS

We would like to thank Professor Xiao-Peng Xing and Professor Chuan-Gang Ning for early contributions to our photoelectron imaging effort. We thank Professor A. G. Suits for valuable discussions concerning the design of the new VMI lens system described in this article. We would like to thank Mr. Ken Talbot and Mr. Randy Goulet of the Chemistry Machine Shop for their invaluable help in the machining of the components for the apparatus, and Mr. Al Tente of the Chemistry Electronic Shop for his invaluable help with the electronics. We acknowledge initial contributions to the construction of the apparatus by Dr. Wei Huang, Dr. Constantin Romanescu, and Dr. Lei Ma. The authors also wish to acknowledge Mr. Drew Morrill for his initial assistance in the data acquisition system. The authors are indebted to Dr. J. R. Gascooke and Dr. Stephen Gibson for their help in the Abel inversion and to Dr. Iñigo Eguskiza for his help with the recursive method coding. We are grateful to Dr. G. Garcia for sharing the pBASEX program and all his recommendations. I.L. would like to thank the Basque Government for a post-doctoral fellowship. This work was supported partially by the National Science Foundation.

¹D. W. Chandler and P. L. Houston, *J. Chem. Phys.* **87**, 1445 (1987).

²H. Helm, N. Bjerre, D. J. Dyer, D. L. Huestis, and M. Saeed, *Phys. Rev. Lett.* **70**, 3221 (1993).

- ³C. Pinare, B. Bagueard, C. Bordas, and M. Broyer, *Phys. Rev. Lett.* **81**, 2225 (1998).
- ⁴A. T. J. B. Eppink and D. H. Parker, *Rev. Sci. Instrum.* **68**, 3477 (1997).
- ⁵H. J. Deyerl, L. S. Alconcel, and R. E. Continetti, *J. Phys. Chem. A* **105**, 552 (2001).
- ⁶E. Surber and A. Sanov, *J. Chem. Phys.* **116**, 5921 (2002).
- ⁷A. V. Davis, R. Wester, A. E. Bragg, and D. M. Neumark, *J. Chem. Phys.* **118**, 999 (2003).
- ⁸G. J. Rathbone, T. Sanford, D. Andrews, and W. C. Lineberger, *Chem. Phys. Lett.* **401**, 570 (2005).
- ⁹M. A. Sobhy and A. W. Castleman, Jr., *J. Chem. Phys.* **126**, 154314 (2007).
- ¹⁰X. P. Xing, X. B. Wang, and L. S. Wang, *Phys. Rev. Lett.* **101**, 083003 (2008).
- ¹¹L. R. McCunn, G. H. Gardenier, T. L. Guasco, B. M. Elliott, J. C. Bopp, R. A. Relph, and M. A. Johnson, *J. Chem. Phys.* **128**, 234311 (2008).
- ¹²C. Bartels, C. Hock, J. Huwer, R. Kuhnen, J. Schwöbel, and B. von Issendorff, *Science* **323**, 1323 (2009).
- ¹³X. Wu, Z. B. Qin, H. Xie, R. Cong, X. H. Wu, Z. C. Tang, and H. J. Fan, *J. Chem. Phys.* **133**, 044303 (2010).
- ¹⁴A. Osterwalder, M. J. Nee, J. Zhou, and D. M. Neumark, *J. Chem. Phys.* **121**, 6317 (2004).
- ¹⁵S. J. Cavanagh, S. T. Gibson, M. N. Gale, C. J. Dedman, E. H. Roberts, and B. R. Lewis, *Phys. Rev. A* **76**, 052708 (2007).
- ¹⁶D. M. Neumark, *J. Phys. Chem. A* **112**, 13287 (2008).
- ¹⁷C. Hock, J. B. Kim, M. L. Weichman, T. I. Yacovitch, and D. M. Neumark, *J. Chem. Phys.* **137**, 244201 (2012).
- ¹⁸X. P. Xing, X. B. Wang, and L. S. Wang, *J. Chem. Phys.* **130**, 074301 (2009).
- ¹⁹C. G. Ning, P. D. Dau, and L. S. Wang, *Phys. Rev. Lett.* **105**, 263001 (2010).
- ²⁰I. León, Z. Yang, and L. S. Wang, *J. Chem. Phys.* **138**, 184304 (2013); **139**, 089903 (2013) (Erratum).
- ²¹Z. Yang, I. León, and L. S. Wang, *J. Chem. Phys.* **139**, 021106 (2013).
- ²²I. León, Z. Yang, and L. S. Wang, *J. Chem. Phys.* **139**, 194306 (2013).
- ²³I. León, Z. Yang, and L. S. Wang, *J. Chem. Phys.* **140**, 084303 (2014).
- ²⁴D. Townsend, M. P. Minitti, and A. G. Suits, *Rev. Sci. Instrum.* **74**, 2530 (2003).
- ²⁵L. S. Wang, H. S. Cheng, and J. W. Fan, *J. Chem. Phys.* **102**, 9480 (1995).
- ²⁶X. B. Wang and L. S. Wang, *Rev. Sci. Instrum.* **79**, 073108 (2008).
- ²⁷L. Ma, K. Majer, F. Chiro, and B. von Issendorff, *J. Chem. Phys.* **131**, 144303 (2009).
- ²⁸L. S. Wang, and X. Li, "Temperature effects in anion photoelectron spectroscopy of metal clusters," in *Proceedings of the International Symposium on Clusters and Nanostructure Interfaces*, Richmond, VA, 25–28 October 1999, edited by P. Jena, S. N. Khanna, and B. K. Rao (World Scientific, River Edge, NJ, 2000), pp. 293–300.
- ²⁹W. Huang and L. S. Wang, *Phys. Rev. Lett.* **102**, 153401 (2009).
- ³⁰W. A. de Heer and P. Milani, *Rev. Sci. Instrum.* **62**, 670 (1991).
- ³¹V. Dribinski, A. Ossadtchi, V. A. Mandelshtam, and H. Reisler, *Rev. Sci. Instrum.* **73**, 2634 (2002).
- ³²G. A. Garcia, L. Nahon, and I. Powis, *Rev. Sci. Instrum.* **75**, 4989 (2004).
- ³³See <http://www.simion.com/> for Simion™.
- ³⁴Wolfram Research, Inc., Mathematica, Version 8.0, Champaign, IL, 2010.
- ³⁵B.-Y. Chang, R. C. Hoetzlein, J. A. Mueller, J. D. Geiser, and P. L. Houston, *Rev. Sci. Instrum.* **69**, 1665 (1998).
- ³⁶W. Li, S. D. Chambreau, S. A. Lahankar, and A. G. Suits, *Rev. Sci. Instrum.* **76**, 063106 (2005).
- ³⁷M. B. Doyle, C. Abeysekara, and A. G. Suits, NuACQ 0.9, see <http://chem.wayne.edu/suitsgroup/NuACQ.html>.
- ³⁸R. C. Bilodeau and H. K. Haugen, *Phys. Rev. A* **64**, 024501 (2001).
- ³⁹E. P. Wigner, *Phys. Rev.* **73**, 1002 (1948).
- ⁴⁰C. E. Moore, *Atomic Energy Levels*, National Bureau of Standards Circular Vol. II (U.S. GPO, Washington, DC, 1971).
- ⁴¹J. Ho, K. Ervin, and W. C. Lineberger, *J. Chem. Phys.* **93**, 6987 (1990).
- ⁴²L. S. Wang, C. F. Ding, X. B. Wang, and S. E. Barlow, *Rev. Sci. Instrum.* **70**, 1957 (1999).
- ⁴³P. D. Dau, H. T. Liu, D. L. Huang, and L. S. Wang, *J. Chem. Phys.* **137**, 116101 (2012).
- ⁴⁴H. T. Liu, C. G. Ning, D. L. Huang, P. D. Dau, and L. S. Wang, *Angew. Chem. Int. Ed.* **52**, 8976 (2013).
- ⁴⁵H. T. Liu, C. G. Ning, D. L. Huang, and L. S. Wang, *Angew. Chem. Int. Ed.* **53**, 2464 (2014).
- ⁴⁶D. L. Huang, P. D. Dau, H. T. Liu, and L. S. Wang, *J. Chem. Phys.* **140**, 224315 (2014).

⁴⁷J. B. Kim, T. I. Yacovitch, C. Hock, and D. M. Neumark, *Phys. Chem. Chem. Phys.* **13**, 17378 (2011).

⁴⁸W. Benjamin, *Imaging in Molecular Dynamics: Technology and Applications* (Cambridge University Press, New York, 2003).

⁴⁹S. Manzhos and H. P. Looock, *Comput. Phys. Commun.* **154**, 76 (2003).

⁵⁰G. M. Roberts, J. L. Nixon, J. Lecointre, E. Wrede, and J. R. R. Verlet, *Rev. Sci. Instrum.* **80**, 053104 (2009).

⁵¹E. W. Hansen and P. L. Law, *J. Opt. Soc. Am. A* **2**, 510 (1985).